ARTICLE

Electrochemical upgrading of biomass-derived 5-hydroxymethylfurfural and furfural over oxygen vacancy-rich NiCoMn-layered double hydroxides nanosheets

Received 00th January 20xx,
Accepted 00th January 20xx

DOI: 10.1039/x0xx00000x

Biying Liu,‡[a] Shaojun Xu,‡[b, c] Man Zhang,[a] Xin Li,[a] Donato Decarolis,[b, c] Yuqian Liu,[a] Yuchen Wang,[a] Emma K. Gibson,[c, d] C. Richard A. Catlow[b, c, d] and Kai Yan*[a]

Rational design of low-cost and active electrocatalysts is crucial for upgrading of biomass-derived chemicals. Here, we report highly efficient catalysts of ternary NiCoMn-layered double hydroxides (NiCoMn-LDHs) nanosheets which are oxygen vacancy-rich, produced under controllable conditions for the electrooxidation of both 5-hydroxymethylfurfural (HMF) to 2,5-furandicarboxylic acid (FDCA) and furfural to furoic acid (FurAc) in mild conditions, respectively. Electrochemical tests showed that the oxidation of HMF and furfural were prior to the oxidation of water at lower applied potentials with NiCoMn-LDHs catalysts. The high yields of FDCA (91.7%) and FurAc (92.4%) were achieved in 2.5 h using 1.15 nm thick NiCoMn-LDHs nanosheets under the optimal condition. The mechanism for the superior performance, high durability, and good Faradaic efficiency has been elucidated by a comprehensive characterization, which confirmed that ultrathin nanosheets expose more Co-NiOOH active sites with oxygen vacancies, facilitating the synergistic effect between HMF and furfural oxidation reaction on Co-Ni and Mn^{2+} states. The oxygen vacancy-rich NiCoMn-LDHs nanosheets catalysts present a novel and energy-efficient solution to obtain upgrading biochemicals.

Introduction

With the diminishing of the limited fossil resources and their associated environmental problems, renewable biomass resource is a promising alternative to generate fine chemicals.[1-3] Among numerous biomass-derived platform chemicals, 2,5-furandicarboxylic acid (FDCA) and furoic acid (FurAc) have attracted considerable attention, as they are important intermediates for the synthesis of widely used polymers, pharmaceuticals, medicine, and fine chemicals.[4, 5] Thus, considerable effort has been devoted to developing active and earth-abundant catalysts to improve the synthesis of FDCA and FurAc. The current commercial process for FDCA and FurAc production is through the selective oxidation of 5-hydroxymethylfurfural (HMF) or furfural at a temperature of over 100 ^{o}C under high-pressure (3 bar - 124 bar) of air or O_2[6, 7] with noble metal-based catalysts (e.g. Au, Pt, Ru, and Pd).[8-12] Kerdi et al. reported that a catalyst of 3.7% Ru impregnated on the active carbon (3.7% Ru_{imp}/AC) promoted the oxidation of HMF with a 25% yield of FFCA and a 75% yield of FDCA after 24 h under the conditions of 100 ^{o}C and 40 bar of air.[13] Douthwaite et al. reported that 1% AuPd/$Mg(OH)_2$ was a highly effective catalyst for the synthesis of FurAc from furfural exhibiting an 87.7% conversion of furfural and 84% yield of FurAc under 3 bar O_2 pressure in 4 h.[14] Although these traditionally catalytic routes have made substantial progress, these approaches require extra air or oxygen at relatively high temperatures using noble metal catalysts. Therefore, it is highly desirable to develop earth-abundant active catalysts to synthesize FDCA and FurAc at ambient pressure and low temperature.

Electrocatalytic oxidation is considered as a green alternative to the traditional catalytic approach, facilitated by adjusting the applied potential to the anode at low temperature and atmospheric pressure, without the need for oxygen or air. Many efforts are invested in the exploitation of efficient catalysts including precious-metal or nonprecious-metal based catalysts to boost the electrooxidation process. For example, Chadderdon et al. found that bimetallic noble-metal based catalysts with different metal ratios showed higher HMF conversion and FDCA selectivity than those of monometallic catalysts, among which, Pd_1Au_2/C achieved 83% selectivity of FDCA in 1 h at 25 ^{o}C under 0.9 V while Pd/C and Au/C catalysts achieved only 29% and 1%, respectively.[15] In consideration of the cost, some transition metal catalysts are also developed with high activity for the oxidation of HMF or furfural that can compete with precious metal catalysts, such as Ni,[16] Ni_2S_3,[17] Ni_2P,[18] Ni_2P/Ni,[19] and Co-P.[20] Unfortunately, they showed poor durability due to the strong metal-oxygen interaction resulting in the formation of metal

---

[a] *Guangdong Provincial Key Laboratory of Environmental Pollution Control and Remediation Technology, School of Environmental Science and Engineering, Sun Yat-sen University, Guangzhou 510275, China.*
[b] *School of Chemistry, Cardiff University, Main Building, Park Place, Cardiff, CF10 3AT, United Kingdom.*
[c] *UK Catalysis Hub, Research Complex at Harwell, Rutherford Appleton Laboratory, Harwell, OX11 0FA, United Kingdom.*
[d] *School of Chemistry, Joseph Black Building, University of Glasgow, Glasgow G12 8QQ, United Kingdom*
[e] *Department of Chemistry, University College London, 20 Gordon Street, London, WC1H 0AJ, United Kingdom*
‡ These Authors contribute equally to this work.
* Corresponding author E-mail: yank9@mail.sysu.edu.cn.

Electronic Supplementary Information (ESI) available: Additional data, experimental details, and supplementary figures including XRD patterns, EPR spectra, Raman spectra, SEM images, XPS spectra, LSV curves, TOF, mass activity, results of conversion and yield, HPLC spectrum, LC-MS spectrum and the proposed oxidation pathway. See DOI: 10.1039/x0xx00000x oxides/hydroxides or the aggregation of nanoparticles. In this context, layered double hydroxides (LDHs), a typical two-dimensional (2D) structure,[21] exhibiting high stability, have attracted much attention.[22, 23] The LDHs comprise cationic plates with hydroxyls and interlayer anions, between which there are strong electrostatic interactions.[24] LDHs with their structural and compositional diversity offer a versatile platform to produce advanced catalysts and are promising for electrocatalysis as reported in our previous work.[25-27] For example, Li et al. reported a one-step method to synthesize NiMn-LDHs (thickness of 1.3 nm) with rich exposure of active metal sites and nearly optimal adsorption energy for intermediates (·OH and ·O), leading to the reduction of 80 mV in the overpotential at 10 mA cm^{-2} compared with that of NiMn-LDHs synthesized by the traditional method.[25] Liu et al. reported that the NiCo-LDHs treated by Ar plasma generated more defects on the surface and presented a lower overpotential of 299 mV at 10 mA cm^{-2} and a smaller Tafel slope of 45 mV dec^{-1} for the oxygen evolution reaction (OER) than that of the pristine materials.[26] Zhang et al. fabricated NiCoFe-LDHs on carbon fiber paper (CFP) for the electrocatalytic oxidation of HMF to FDCA resulting in 95.5% conversion of HMF and 84.9% selectivity of FDCA in 1 h.[27] Although many studies have significantly advanced the field of electrocatalytic oxidation of HMF or furfural, there are still relatively few studies that have focused on the synthesis of earth-abundant ternary LDH nanosheets for electrochemical oxidation, especially relating to the versatility for both HMF and furfural. An additional factor that needs to be addressed is that the low current density induced by the competition of water oxidation at the anode which remains a significant barrier for the production of fine chemicals.

Here we report the highly efficient electrocatalytic oxidation of HMF to FDCA and furfural to FurAc using the readily synthesizable NiCoMn-LDH nanosheets which are oxygen vacancy-rich loaded on Ni foam (NF). The NiCoMn-LDHs/NF with different metal ratio were denoted as NiCoMn(1:1)-LDHs/NF, NiCoMn(2:1)-LDHs/NF and NiCoMn(3:1)-LDHs/NF, corresponding to (Ni^{2+} and Co^{2+})/Mn^{2+} ratio of 1:1, 2:1 and 3:1, respectively. The effect of metallic NiCo:Mn ratios of NiCoMn-LDHs on the catalytic activity was studied to optimize the catalyst composition. Comprehensive characterization was performed to elucidate the relationship between catalyst structure and performance. Different metal ratios, reaction temperatures, and reactant concentrations were investigated systemically to optimize the yields of FDCA and FurAc. Also, reaction kinetics, electrochemical oxidation, and reaction pathways were studied and proposed. Our results offer a new route to utilize low-cost and active LDHs for the electrochemical synthesis of valuable fine chemicals.

Experimental

Synthesis of NiCoMn-LDHs nanosheets.

Mixed Ni^{2+}, Co^{2+}, and Mn^{2+} solutions were prepared according to the pre-calculated ratios (solution A). The compositions of the mixed solutions are summarized in Table S1. 1 M NaOH and 0.1 M Na_2CO_3 were blended with the volume ratio of 4:1 to achieve solution B. Solution A and B were then slowly titrated into a four-necked round flask to adjust the pH value to 8.5 with 1200 rpm stirring and held for 1 h. Next, the solution was transferred to the hydrothermal vessel with a 1 cm × 1 cm pre-purged piece of Ni foam (NF). After being heated at 100 °C for 12 h, the reactor was opened cooled to room temperature. The resulting NiCoMn-LDHs/NF and powders collected from the remaining solution by centrifugation were dried in a vacuum at 80 °C for 8 h. The sources of chemical reagents used in this work are given in Table S2. No unexpected or unusually high safety hazards were encountered.

Electrochemical oxidation of HMF and furfural.

An electrochemical workstation (Metro Autolab M204, Utrecht, The Netherlands) was applied to initiate the electrochemical oxidation of HMF and furfural. The oxidation occurred in an H-cell under a rotating rate of 500 rpm with aqueous 1 M NaOH (pH=13.5) containing different concentrations of HMF or furfural. A standard three-electrode system was built up as follows: the as-prepared NiCoMn-LDHs/NF was the working electrode (anode), an Ag/AgCl electrode as the reference electrode, and a Pt-wire electrode as the counter electrode (cathode). A nafion 117 membrane was then utilized to separate the two chambers of anode and cathode. The potential of the Ag/AgCl electrode was converted towards the potential of reversible hydrogen electrode (RHE) based on the Nernst equation.

High-performance liquid chromatography (HPLC, Shimadzu Prominence SIL-20A) and liquid chromatograph-mass spectrometer (LC-MS, UltiMate3000-timsTOF) were used to detect the specific concentration of HMF, furfural, and other products. The ultraviolet-visible detector was set at 265 nm, 5 mM ammonium formate and chromatography methanol served as the mobile phase A and mobile phase B in the proportion of 30%/70% with a constant flow rate of 1 mL min^{-1}. The temperature was controlled at 40 °C and the volume of each injected sample was 10 μL. The conversion of HMF ($\boldsymbol{Conv_{HMF}}$) and furfural ($\boldsymbol{Conv_{Fur}}$) and the yields of oxidation product ($\boldsymbol{Y_{FDCA}}$) and ($\boldsymbol{Y_{FurAc}}$) are calculated as follows:

$$\boldsymbol{Conv_{HMF} = \left(1 - \frac{C_{HMF}}{C_{0-HMF}}\right) \times 100\%}$$

$$\boldsymbol{Conv_{Fur} = \left(1 - \frac{C_{Fur}}{C_{0-Fur}}\right) \times 100\%}$$

$$\boldsymbol{Y_{FDCA} = \frac{C_{FDCA}}{C_{0-HMF}} \times 100\%}$$

$$\boldsymbol{Y_{FurAc} = \frac{C_{FurAc}}{C_{0-Fur}} \times 100\%}$$

where, $\boldsymbol{C_{HMF}}$ and $\boldsymbol{C_{0-HMF}}$ are the instant and initial concentration of HMF, respectively; $\boldsymbol{C_{Fur}}$ and $\boldsymbol{C_{0-Fur}}$ are the instant and initial concentration of furfural, respectively; and $\boldsymbol{C_{FDCA}}$ and $\boldsymbol{C_{FurAc}}$ are the instant concentration of FDCA and FurAc, respectively. All the units of concentration are mmol L^{-1} (mM). Additionally, the procedures relating to the Nernst equation, Debye-Scherrer equation, turnover frequency (TOF) calculation, mass activity calculation, and Faradaic efficiency are shown on page S4 to page S5 in the Supporting information.

Results and discussion

Characterization of NiCoMn-LDHs nanosheets.

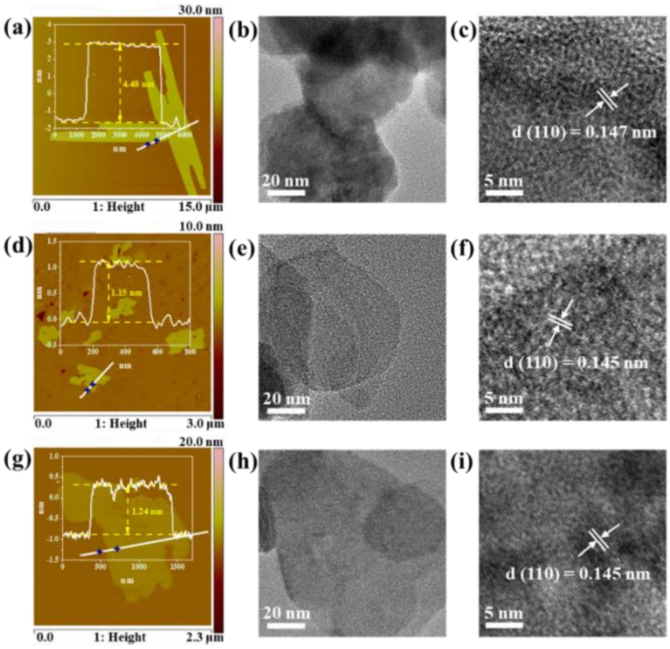

Figure 1. AFM images and the corresponding height profile as well as the TEM and HR-TEM images of powder NiCoMn-LDHs: (a-c) NiCoMn(1:1)-LDHs, (d-f) NiCoMn(2:1)-LDHs and (g-i) NiCoMn(3:1)-LDHs.

Samples of NiCoMn-LDHs with different NiCo:Mn ratios were produced using the co-precipitation method under ambient conditions and hydrothermal treatment (loading mass of ~0.5 mg cm^{-2}). X-ray diffraction (XRD) (Figure S1a) confirmed the crystalline phase of the NiCoMn-LDHs/NF with different ratios of (Ni^{2+} and Co^{2+}) versus Mn^{2+} (1:1, 2:1 and 3:1) with characteristic exfoliated LDHs phases for (003), (006), (012) and (110) crystal planes.[28, 29] A peak shift at low 2ϑ between 10° and 20° of NiCoMn-LDHs with different NiCo:Mn ratios was noticed because of the changes in the interlayer spacing (d) (Table S3), which could be ascribed to the replacement by Mn with a larger ionic radius (0.80 nm) for Ni (radius, 0.69 nm) and Co (radius, 0.72 nm) sites in the NiCoMn-LDHs nanosheets.[29, 30] The d-spacing value of the basal plane (~0.75 nm) suggested that CO_3^{2-} served as the intercalating anions.[31] These effects were reflected in changes in the *a* and *c* parameters of the unit cell of LDHs which varied with the metal ratio (Figure S1b). The *a* value increased concomitantly with Mn level as a consequence of the addition of Mn in place of Ni- or Co-lattice sites, while the NiCoMn(2:1)-LDHs/NF had the smallest *c* value due to an increase in the charge of the hydroxide layers.[32] Moreover, the average crystallite size (D) calculated by the Debye-Scherrer equation from (003) peak (Table S3) of NiCoMn-LDHs/NF with different NiCo:Mn ratios of 1:1, 2:1 and 3:1 was 20.726 nm, 19.968 nm, and 21.627 nm, respectively. In addition, the elemental analysis further confirmed the metal ratios by inductively coupled plasma optical emission spectroscopy (ICP-OES) (Table S4).

The specific thickness of the as-synthesized NiCoMn-LDHs materials with different metal ratios was further characterized using atomic force microscopy (AFM). The corresponding height profile was inset in the AFM images. The thickness of NiCoMn(2:1)-LDHs was 1.15 nm (Figure 1d), which was slightly larger than the basal spacing of LDHs (i.e. 0.75 nm). The deviation in thickness of ~0.4 nm may be ascribed to the possible adsorption of water molecules as well as counteranions on the surface of the nanosheets.[33, 34] The NiCoMn(3:1)-LDHs samples with the thickness of 1.24 nm (Figure 1g) and NiCoMn(1:1)-LDHs with the thickness of 4.48 nm (Figure 1a) thus comprised about 2-6 lamellar layers.[35, 36]

Transmission electron microscopy (TEM) images further confirmed that the ultrathin and rhombohedral LDH nanosheets were successfully produced. NiCoMn(2:1)-LDHs (Figures 1e and 1f) and NiCoMn(3:1)-LDHs (Figures 1h and 1i) presented thinner and more transparent features with a thinner lattice spacing of 1.45 Å indexed to the (110) planes, which was consistent with the result of XRD and AFM. Compared to the NiCoMn(2:1)-LDHs and NiCoMn(3:1)-LDHs, the NiCoMn(1:1)-LDHs displayed wider lattice spacing of 1.47 Å assigned to the (110) planes (Figures 1b and 1c). Again, the increasing replacement of Ni and Co by Mn which has a larger ionic radius, 0.8 nm compared to 0.69 and 0.72 nm for Ni and Co, respectively, in the NiCoMn-LDHs accounts for this above phenomenon.

To investigate the surface oxygen vacancies (O_v) in the fabricated LDHs, electron paramagnetic resonance (EPR) was employed (Figure S2). NiCoMn-LDHs displayed a strong symmetrical EPR signal at g = 2.002, which can be assigned to the paramagnetic O_v.[37] Moreover, the NiCoMn(2:1)-LDHs had the strongest EPR signal manifesting a sufficient amount of O_v, which had been proven to be an excellent and effective way to facilitate the electron transport capacity and superior electrooxidation performance in transition metal catalysts.[38] In addition, the presence of oxygen vacancies can also decrease the coordination number, which benefits the adsorption of HMF and furfural molecules onto the surface of the catalyst, since the low-coordinated surface has a large concentration of active sites and better catalytic activity.[39] Therefore, HMF and furfural molecules would be preferentially adsorbed on the surface with oxygen vacancies to reduce their adsorption energy.[40]

A detailed investigation of the local structure of the metal cations was undertaken by analysis of the extended X-ray absorption fine structure (EXAFS) region of the XAFS data collected at the Ni K-edge, Co K-edge, and Mn K-edge. The EXAFS data of the Ni K-edge (Figures 2a and 2b) can be fitted to two scattering paths, one that can be assigned to Ni-O and the other due to a Ni-M (M = Ni, Co, Mn) scattering path at 2.04 and 3.06 Å, respectively. The fit results from this edge suggested that each Ni only connected to O and to a M both with the coordination number (CN) of 8 (Table S5). Whether the M was Ni, Co or Mn cannot be extracted from the data, due to the similar scattering factor of the elements. Fitting the Mn-K edge data (Figures 2e and 2f) revealed the presence of at least two shells. The first shell was a Mn-O with a distance of 1.91 Å and the CN was ~4. The second shell was attributed in a first approximation to a Mn-Mn scattering, with a distance of 3.02 Å and coordination of ~9 (Table S7). However, the EXAFS data showed various oscillations at a higher k range (between 9 and 12 $Å^{-1}$) for which the fit of a simple Mn-Mn scattering path was not sufficient. Therefore, it was possible that multiple shells were presented in the region between 2.00 and 3.50 Å, which can be attributed to a different metal, either Co or Ni, which can also be inferred by examining the Fourier transform, where another shell can be seen at ~3.25 Å. The possibility of this longer distance scattering due to a Mn-O scattering path of MnO, has been excluded as this feature increases in intensity with increasing k-weight, a sign of this scattering being due to heavy element. However, fitting of multiple shells containing atoms with close scattering contributions was not possible due to the short-range of the EXAFS, however, the understanding of these contributions can be understood by an analysis of the EXAFS of the Ni and Co, similar to the study performed by Zhang.[41] Indeed, two shells could be found in analyzing the XAFS of the Co K-edge (Figures 2c and 2d). The Co-O distance was significantly short compared to the one of Ni (1.90 Å compared to 2.00 Å) with a much lower CN of 5 (Table S6), suggesting that the nature of the Co cation is more akin Mn than Ni. However, examining the second shell, it was noted that the distance of this Co-M (M = Co, Ni, Mn) was significantly larger than that observed with either Mn or Ni (3.39 Å compared to 3.02 Å). Combining these results with the information obtained from the Mn K edge, it was possible to surmise that the shell which could not be extracted from the Mn K edge may be attributed to a Mn-Co scattering.

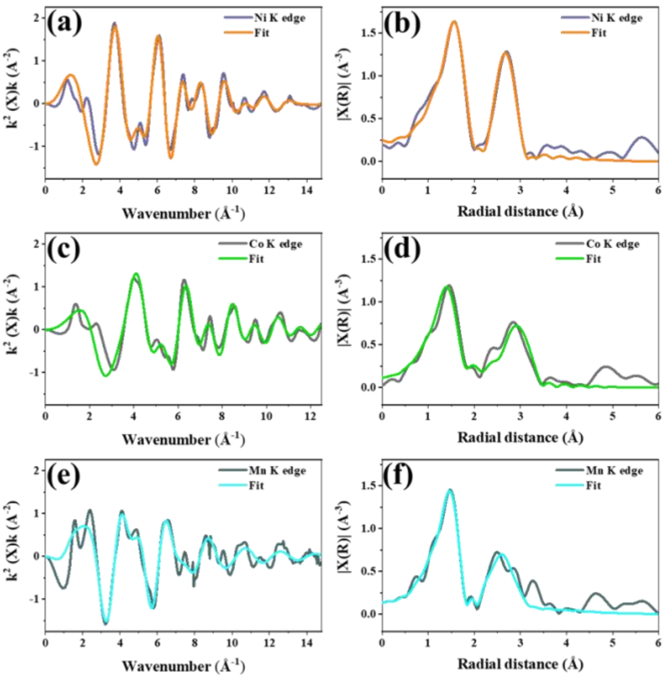

Figure 2. (a) Ni K-edge EXAFS oscillation functions $k^2\chi(k)$ and (b) the corresponding magnitude of the Fourier Transform. (c) Co K-edge EXAFS oscillation functions k2χ(k) and (d) the corresponding magnitude of the Fourier Transform. (e) Mn K-edge EXAFS oscillation functions k2χ(k) and (f) the corresponding magnitude of the Fourier Transform.

Raman spectroscopy was further used to investigate the surface bond formation of the fabricated LDHs and the spectra were shown in Figure S3. The band at 611 cm^{-1} was assigned to the hexagonal U_{MO6} vibration (M = Mn cations, A_{1g} mode).[42, 43] With the increased Mn content, the area of U_{MO6} vibration rose. It was reported that the band ranging from 445 to 465 cm^{-1} was assigned to the Ni-O vibration of α-$Ni(OH)_2$ and β-$Ni(OH)_2$.[44] The disordered or doped $Ni(OH)_2$ showed a Ni-O vibration that was shifted to a higher wavenumber. Therefore, the band at 480 cm^{-1} in NiCoMn(3:1)-LDHs was ascribed to the defective or disordered $Ni(OH)_2$. The band at 495 cm^{-1} in NiCoMn(1:1)-LDHs and NiCoMn(2:1)-LDHs indicated higher levels of a defective or disordered structure as observed in $Ni(OH)_2$.[44] Moreover, the band at 527 cm^{-1} indicated the presence of a Co-O symmetric stretching mode.[45] In addition, the area of the Co-O band varied with different ratios of incorporated Mn cations, revealing a change in the local environment of Co-O. With all the information obtained by the different characterization techniques, ultrathin and rhombohedral LDH nanosheets with high levels of $Ni(OH)_2$ defects were successfully produced.

The electrochemical performance of NiCoMn-LDHs nanosheets.

As NiCoMn(2:1)-LDHs possessed a unique structure, this material was selected as the anode to evaluate the electrochemical performance in the different electrolytes (1 M NaOH with and without HMF and furfural) with a standard three-electrode system. Linear sweep voltammetry (LSV) was investigated to evaluate the performance of LDHs nanosheets under the scan rate of 3 mV s^{-1}. Figure 3a showed that NiCoMn-LDHs/NF had much higher activity in 1M NaOH with HMF and furfural than in pure 1 M NaOH electrolytes. The overpotential of NiCoMn-LDHs/NF required to reach a current density of 50 mA cm^{-2} for the oxidation of furfural and HMF was 350 mV and 370 mV, whilst the overpotential was 410 mV for the oxidation of water. The LSV curves of pure NF were also studied as a benchmark and shown in Figure S4. As was shown, the electrochemical activity, using pure NF was clearly much lower than that observed for the NF with NiCoMn-LDHs. The results indicated that the NiCoMn-LDHs played an important role in the oxidation reaction. In addition, the onset potential of NiCoMn-LDHs/NF in 1 M NaOH with HMF and furfural was ~ 1.42 V, 30 mV less than those in pure 1 M NaOH electrolytes (1.45 V). The tendency towards lower potential of the curves indicated that the oxidation of HMF and furfural occurred with lower potential in comparison with that for water oxidation. In addition, Tafel plots were used to study the reaction kinetics. The Tafel slopes (Figure 3b) were 118 and 112 mV·dec^{-1} for the oxidation of HMF and furfural, respectively, which were much lower than that of 145 mV dec^{-1} for water oxidation, further indicating the faster electrocatalytic kinetics for the oxidation of HMF or furfural compared with that for water oxidation.

Electrochemical impedance spectroscopy (EIS) was used to probe the relevant Nyquist plots with the frequency ranging from 0.01 Hz to 10^5 Hz at the open circle voltage. As shown in Figure 3c, the solution resistance (R_Ω) was ~0.85 Ω in furfural solution and ~0.95 Ω in HMF solution, lower than that in pure alkaline solution (~1.34 Ω). At the same time, the charge-transfer resistances (R_{ct}) of NiCoMn-LDHs/NF in different electrolytes were all lower than 1.0 Ω. The NiCoMn-LDHs/NF in furfural and HMF solution gave the smallest R_{ct} of ~0.30 Ω, while the R_{ct} in pure alkaline solution was ~0.60 Ω. The EIS further revealed that the electron transportation in furfural and HMF solution was faster than that in pure alkaline solution.

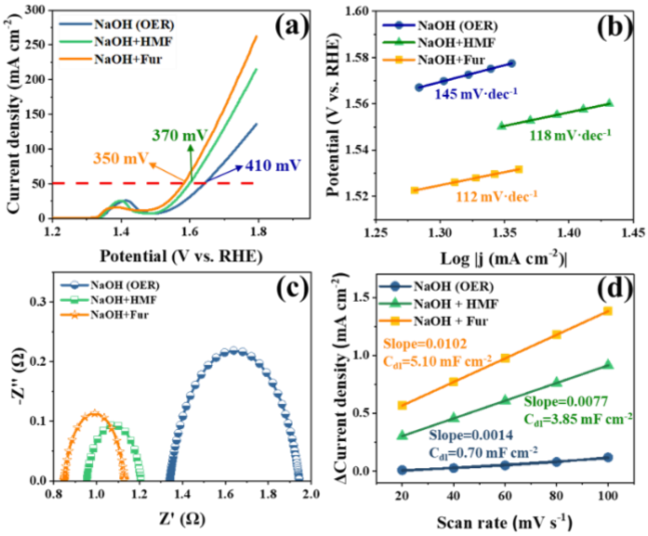

Figure 3. (a) LSV curves, (b) Tafel plots, (c) Nyquist plots of impedances, and (d) change of current density plotted against the scan rate of NiCoMn(2:1)-LDHs/NF in different electrolytes §.
§ Reaction details: 1 M NaOH, 1 M NaOH with 1 mM HMF, and 1 M NaOH with 1 mM furfural (abbreviated as "Fur" in figures and tables).

Moreover, the electrochemical surface area (ECSA) in different electrolytes was assessed by the electrochemical double layer capacitance (C_{dl}). C_{dl} was obtained by cyclic voltammetry (CV) ranging from 1.15 - 1.25 V at different scan rates (20, 40, 60, 80, and 100 mV s^{-1}). As shown in Figure 3d, NiCoMn-LDHs/NF in furfural solution possessed the largest C_{dl} of 5.10 mF cm^{-2} while the C_{dl} in HMF solution was 3.85 mF cm^{-2}, which was significantly higher than that in pure alkaline solution (0.70 mF cm^{-2}). The higher effective surface area in furfural and HMF solutions led to the decline of overpotential and the enhancement of oxidation performance. In addition, we also compared the reaction kinetics in different electrolytes using the turnover frequency (TOF) and mass activity (Figures S5a and S5b). Under the overpotential of 400 mV, the NiCoMn-LDHs/NF in furfural solution exhibited a superior TOF of 0.081 s^{-1} and high mass activity of 0.181 A mg^{-1}, which was much higher than that in HMF solution (0.044 s^{-1} and 0.147 A mg^{-1}) and in pure alkaline solution (0.040 s^{-1} and 0.090 A mg^{-1}), respectively.

Factors influencing the upgrading of HMF.

Different factors including temperature, reactant concentration, and metal ratios were systematically investigated to optimize the selectivity of high-valued products FDCA. The NiCoMn(2:1)-LDHs/NF at a fixed potential of 1.50 V at a stirring speed of 500 rpm was used. In terms of the reaction temperature, the electrochemical oxidation of 1 mM HMF in 1 M NaOH was carried out at different temperatures (25 °C, 35 °C, 45 °C, and 55 °C). As can be seen in Figure 4a, the conversion of HMF reached 100% in 150 min (except for at 25 °C), showing that increasing temperature helped the conversion of HMF. As shown in Figure 4b, the highest yield of FDCA at 35 °C reached 91.7% in 150 min, whilst that at 25 °C of 72.9%, 45 °C of 42.3%, and 55 °C of 16.3%. The oxidation of HMF was an exothermic reaction. The Gibbs free energy change (△G) from HMF to HMFCA was 1.48 eV while the △G from HMF to DFF was 1.85 eV.[46] Increasing temperature was conducive to the progress of reaction. However, the enhancement was limited in exothermic reaction due to the suppression of positive reaction and encouragement of reverse reaction by high temperature. Therefore, the optimized temperature of 35 °C was chosen in this study.

The effect of reactant concentration was studied for the electrochemical oxidation reaction, varying the HMF concentration (1 mM, 5 mM, 10 mM, and 20 mM) with 1 M NaOH was studied at 35 °C. From Figure 4c, 1 mM and 5 mM HMF electrolytes acquired 100% conversion of HMF in 90 min, while conversion of 10 mM HMF was 41.5% and 20 mM was 31.4%, respectively. The best performance with 81.4% yield of FDCA in 90 min using 1 mM HMF, which was much higher than that in 5 mM (31.2%), 10 mM (9.5%) and 20 mM (7.1%) (Figure 4d). With the increased HMF concentration, the yield of FDCA fallen dramatically, as the humin type products formed from HMF on the electrode surface during electrolysis hindered the electrochemical oxidation.

Different ratios of (Ni^{2+} and Co^{2+}) to Mn^{2+} were studied to optimize the catalyst composition for the electrochemical HMF oxidation. Catalysts with three ratios of (Ni^{2+} and Co^{2+}) to Mn^{2+} (1:1, 2:1, and 3:1) were tested at the optimal temperature of 35 °C and HMF concentration of 1 mM. As shown in Figures 4e and 4f, NiCoMn-LDHs/NF with different metal ratios all attained 100% HMF conversion in 150 min. NiCoMn(2:1)-LDHs/NF achieved the highest

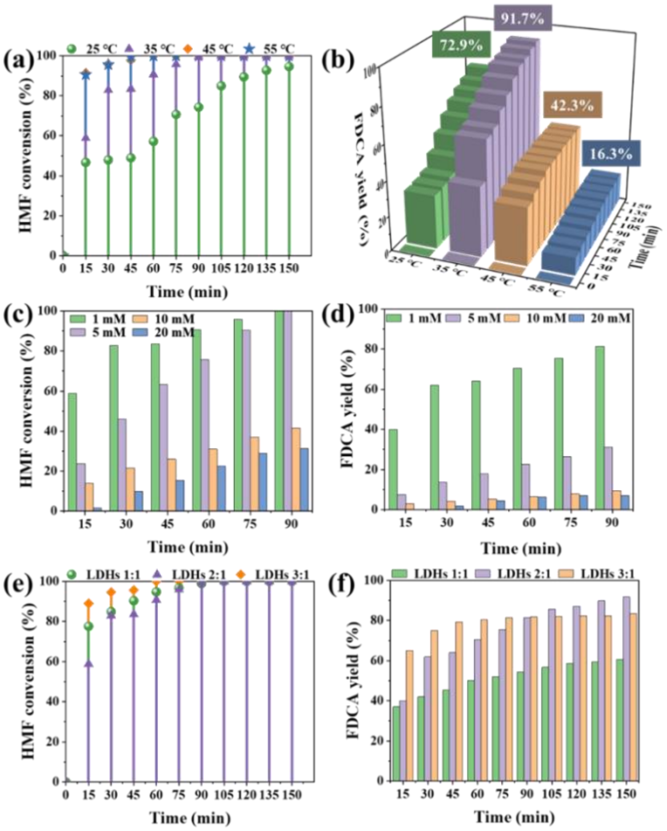

Figure 4. (a) The conversion of 1 mM HMF and (b) the yield of FDCA in different temperatures (25 °C, 35 °C, 45 °C, and 55 °C). (c) The conversion of different concentrations of HMF (1 mM, 5 mM, 10 mM, and 20 mM) and (d) the yield of FDCA at the temperature of 35 °C. (e) The conversion of 1 mM HMF and (f) the yield of FDCA at the temperature of 35 °C by using NiCoMn(1:1)-LDHs/NF, NiCoMn(2:1)-LDHs/NF and NiCoMn(3:1)-LDHs/NF.

FDCA yield of 91.7%, which was much higher than that achieved over NiCoMn(3:1)-LDHs/NF (83.6%) and NiCoMn(1:1)-LDHs/NF (60.2%). Here, the stoichiometric amount of charge required to completely convert 35 mL 1 mM HMF to FDCA was 20.3 C. Therefore, the Faradaic efficiency of FDCA was ~65% when 20.3 C charge was passed over NiCoMn(2:1)-LDHs/NF catalysts at 35 °C and 1 mM HMF concentration. Compared to the results (Table S8) in the literature, it shows the performance obtained here with complete conversion of 1 mM HMF and 91.7% yield of FDCA under 35 °C is exceptional.

Factors influencing the oxidation of furfural.

To investigate how the optimal reaction parameters influenced the electrocatalytic upgrading of furfural, NiCoMn(2:1)-LDHs/NF at a fixed potential of 1.50 V was chosen for further investigation. To investigate the effect of temperature, the electrochemical oxidation of 1 mM furfural with 1 M NaOH was studied for a temperature range of 25 °C to 55 °C. For all temperatures, the almost complete conversion of furfural was reached after 2 h (Figure 5a). The oxidation of furfural was also an exothermic reaction. Similarly, excessive temperature can prevent the forward reaction of furfural oxidation. As with HMF, the optimal temperature for the highest yield of FurAc (92.4%) was 35 °C (Figure 5b).

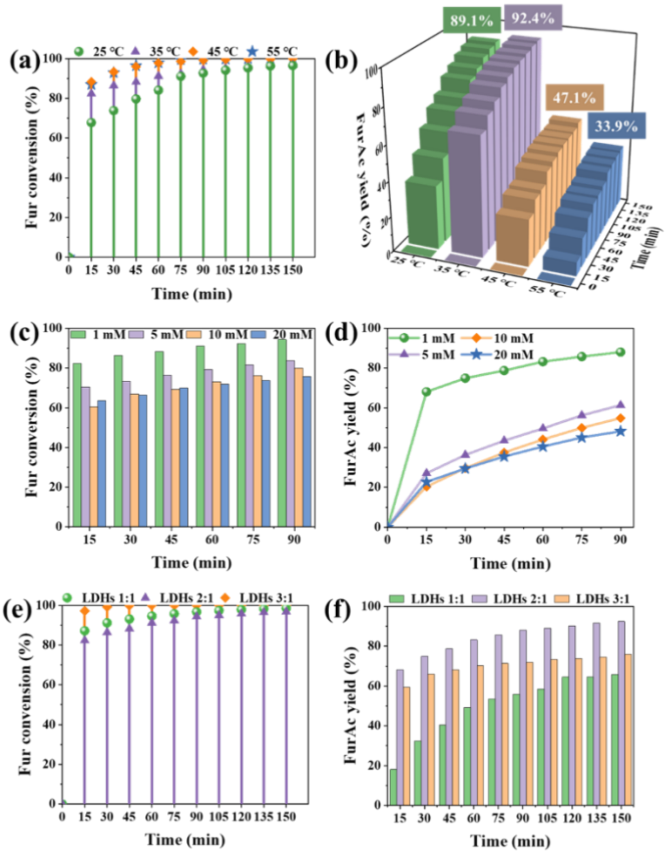

Figure 5. (a) The conversion of 1 mM furfural and (b) the yield of FurAc at different temperatures. (c) The conversion of different concentrations of furfural and (d) the yield of FurAc at 35 °C. (e) The conversion of 1 mM furfural and (f) the yield of FurAc at temperature of 35 °C by using NiCoMn(1:1)-LDHs/NF, NiCoMn(2:1)-LDHs/NF and NiCoMn(3:1)-LDHs/NF.

The reactant concentration influence on the catalytic performance was further explored. The concentration of furfural in the range of 1 mM to 20 mM was studied at 35 °C and the catalytic results were depicted in Figures 5c and 5d. 1 mM furfural electrolyte achieved the highest conversion of furfural (94.3%) and yield of FurAc (88.0%) in 90 min. The influence of reactant concentration on the yield of FurAc showed a similar trend to that obtained with HMF. The reason was that the facile oxidation from FurAc towards surface bond furoate, which can give rise to an ordered monolayer by accumulation and block the catalysts surface, avoiding the production of FurAc.[47]

NiCoMn-LDHs/NF with different NiCo:Mn ratios (1:1, 2:1 and 3:1) were also investigated under the optimal conditions of 35 °C and 1 mM reactant. Figure 5e showed that the conversion of furfural achieved almost full conversion in 150 min by NiCoMn-LDHs/NF for all ratios. NiCoMn(2:1)-LDHs/NF catalyst still gave the best activity for furfural oxidation with the predominant FurAc yield of 92.4% in 150 min, while FurAc yield of 65.8% and 76.0% in 150 min by NiCoMn(1:1)-LDHs/NF and NiCoMn(3:1)-LDHs/NF (Figure 5f), respectively. The charge of 13.5 C was theoretically needed to transform 35 mL 1 mM furfural into FurAc thus the Faradaic efficiency was ~70% by NiCoMn(2:1)-LDHs/NF catalysts at 35 °C and 1 mM furfural concentration. Overall, the oxidation of furfural resulted in higher yields of the target product than that was found for HMF, which correlated with the results of the electrochemical performance. The pure NF was also used for the oxidation of HMF and furfural to clarify a differentiated contribution between NiCoMn-LDHs and NF. As shown in Figure S6, NF had 15.2% conversion for HMF and 15.8% conversion for furfural, while the yield of FDCA and FurAc was 2.4% and 2.5% in 150 min, respectively. It was demonstrated that the pure NF had a slight influence on the conversion of HMF and furfural and hardly any selectivity towards FDCA and FurAc.

All the results of oxidation of HMF and furfural in different reaction condition parameters including temperatures, reactant concentrations, and metal ratios of LDHs, are listed in Table S9-S11. Comparisons of the oxidation of HMF and furfural catalyzed by different anodic catalysts in alkaline electrolytes from previous reports are summarized in Table S8. The results clearly show the benefits of the NiCoMn-LDHs nanosheets synthesized in this work.

The stability of NiCoMn-LDHs.

The LSV curves were utilized in a four-necked round flask to study the durability of the catalysts. As Figure S7 shows, the NiCoMn(2:1)-LDHs/NF before and after biomass oxidation displayed good reproducibility of the polarization curves. During four cycles of HMF to FDCA and furfural to FurAc electrolysis, the NiCoMn(2:1)-LDHs/NF retained over 90% HMF and furfural conversion and over 85% FDCA and FurAc in Figure S8. Moreover, from the XRD analysis of the used catalysts (Figure S9), the patterns after oxidation reaction displayed the characteristic peaks of LDHs, as with the fresh catalysts, demonstrating that the LDHs remained stable. Additionally, scanning electron microscopy (SEM) was used to observe any morphological variation of NiCoMn(2:1)-LDHs/NF before and after the oxidation reaction of HMF and furfural. As shown in Figure S10, the morphology and structure remained stable retaining the rhombohedral nanosheets, which confirmed the high stability of the structure and morphology.

The stability of the NiCoMn(2:1)-LDHs/NF before and after the oxidation reaction of HMF and furfural was additionally characterized using X-ray Photoelectron Spectroscopy (XPS). The binding energy was listed in Table S12. The XPS full spectra (Figure 6a) showed similar peaks to those observed for the fresh electrode. In the Ni 2p region (Figure 6c), the binding energies at 855.3 eV and 873.0 eV (Ni $2p_{3/2}$ and Ni $2p_{1/2}$, respectively) with two shakeup satellites (879.8 eV and 861.5 eV, respectively) corresponded to Ni^{2+} from $Ni(OH)_2$, whereas the binding energies at 857.1 eV and 874.7 eV (Ni $2p_{3/2}$ and Ni $2p_{1/2}$, respectively) were assigned to the small amount of Ni^{3+} from NiOOH in the samples.[48] After the reaction, the intensity of NiOOH increased as $Ni(OH)_2$ was oxidized to NiOOH, which has been reported to be the direct active mediator in the oxidation reaction.[49] For the Co 2p spectra (Figure 6d), two main peaks after oxidation of HMF (Co $2p_{3/2}$ peak at 780.9 eV with a satellite peak at 786.5 eV and Co $2p_{1/2}$ peak at 796.6 eV with satellite peak at 802.7 eV) and furfural (Co $2p_{3/2}$ peak at 780.9 eV with satellite peak at 787.3 eV and Co $2p_{1/2}$ peak at 796.6 eV with satellite peak at 804.0 eV) both shifted to higher binding energy compared with the fresh electrode (Co $2p_{3/2}$ peak at 780.7 eV with satellite peak at 785.5 eV and Co $2p_{1/2}$ peak at 796.3 eV with satellite peak at 802.5 eV).[50] These observations may suggest that some of the Co formed stronger interactions with the intermediates.[51] As for Mn, the Mn $2p_{3/2}$ signal composed of two separate peaks centered at 641.9 eV and 643.6 eV and Mn $2p_{1/2}$ signal centered at 654.0 eV in the fresh NiCoMn(2:1)-LDHs/NF, suggested the presence of Mn^{3+} and Mn^{2+} in the samples (Figure 6b).[52] After HMF and furfural oxidation, Mn $2p_{3/2}$ and Mn $2p_{1/2}$ peaks shifted to higher binding energy, whereas the atomic Mn^{2+} concentration decreased and the Mn^{3+} concentration increased. These results proved that the inter-conversions between Mn ions on the surface of catalyst took place during the oxidation of HMF and furfural, resulting in the continuous activation for the faster conversion towards target products.

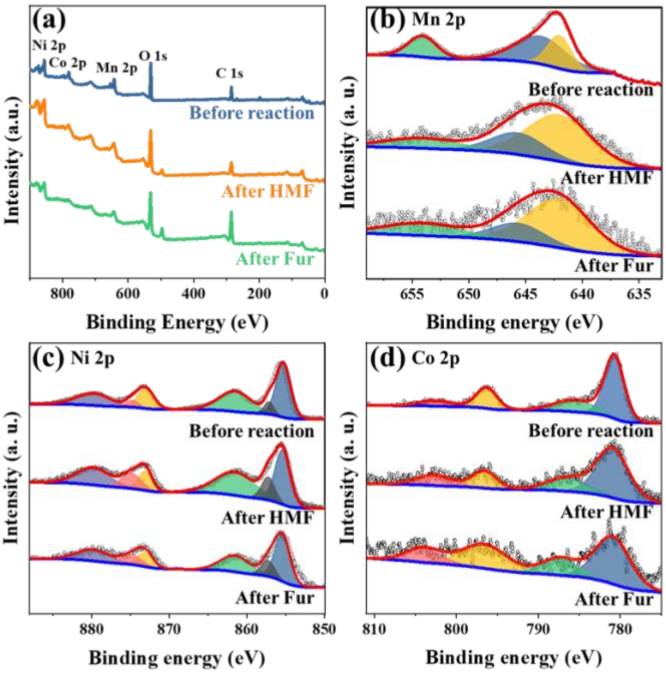

Figure 6. (a) XPS full spectra, (b) Mn 2p, (c) Ni 2p spectra and (d) Co 2p spectra of NiCoMn(2:1)-LDHs/NF before and after the oxidation reaction.

Oxidation pathways.

Apart from the main product FDCA and FurAc from the oxidation reaction of HMF and furfural, some by-products were observed, namely 5-hydroxymethyl-2-furancarboxylic acid (HMFCA), 5-formyl-2-furancarboxylic acid (FFCA), and 2,5-diformylfuran (DFF), determined by high-performance liquid chromatography (HPLC) as shown in Figure S11. Liquid chromatograph-mass spectrometer (LC-MS) was further conducted to verify the intermediate products during the oxidation of HMF in Figure S12. Based on the above experimental results, a schematic diagram of the electrocatalytic oxidation process of HMF on NiCoMn-LDHs/NF was proposed in Figure S13. Two possible reaction pathways for the electrochemical oxidation of HMF occurred in alkaline solution which agreed with the pathway proposed previously.[53] According to the XPS analysis of NiCoMn(2:1)-LDHs nanosheets before and after reaction, the oxidation step (HMF→DFF) from the first pathway proceeded through the inter-conversions between Mn ions on the surface of catalysts. Some Mn^{2+} ions could be oxidized into Mn^{3+} in the electrooxidation process. The alcohol chain in HMF was dehydrogenated to form an aldehydic group in combination with the transformation of Mn^{3+} to Mn^{2+}. Then, an original diol was produced by nucleophilic addition of the hydroxide ions and a proton transferred from the aldehydic group in DFF. Oxygen vacancies can enhance the electrolyte wettability and the coordinate hydroxyls of the catalysts surface. With the aid of the adequate coordinate hydroxyls on the catalysts surface, the unstable diol was transformed into FFCA by dehydrogenation. In the other pathway, the HMF was converted to FFCA through HMFCA by a succession of sequential hydration and dehydrogenation steps with rich covalent of Mn ions and oxygen vacancies. The second main intermediate gave FFCA from DFF and HMFCA, further proceeding to the target product of FDCA by the similar formation of aldehyde and dehydrogenation of idol. Based on the HPLC (Figure S14) and LC-MS results (Figure S15), the possible reaction pathway of electrocatalytic oxidation of furfural was also proposed in Figure S16. The furfural was swiftly and directly turned into FurAc with no detectable intermediates through the similar hydration and dehydrogenation reaction under the impetus of rich covalent of Mn ions and oxygen vacancies.[54]

Conclusions

In conclusion, we have successfully developed a facile method to synthesize the ultrathin and rhombohedral NiCoMn-LDHs/NF efficient for the direct electrochemical oxidation of HMF and furfural towards FDCA and FurAc, respectively. A series of electrochemical measurements revealed that electrocatalytic oxidation of HMF and furfural had an excellent dynamic performance with very low overpotential at 50 mA cm^{-2} (370 mV for HMF and 350 mV for furfural) and high catalytic activity. The small Tafel slope in HMF (118 mV dec^{-1}) and furfural (112 mV dec^{-1}) proved the dominance of these reactions over the oxidation of water (410 mV at 50 mA cm^{-2} and 145 mV dec^{-1}). The R_{ct} of NiCoMn-LDHs/NF in HMF and furfural solution was reduced by ~0.3 Ω than that in water oxidation. The C_{dl} had a strong improvement in furfural (5.10 mF cm^{-2}) and HMF (3.85 mF cm^{-2}) in comparison with water oxidation (0.70 mF cm^{-2}). The TOF and mass activity had an ~80% and 50% increase in furfural and HMF, respectively, than that in pure alkaline solution. The highest yield of FDCA and FurAc was 91.7% and 92.4% in 150 min, respectively, by using NiCoMn(2:1)-LDHs/NF under the optimal condition of 35 ^{o}C and 1 mM reactant. The Faradaic efficiency in optimal reaction conditions was ~65% in HMF and ~70% in furfural. In addition, the potential oxidation pathways for HMF and furfural were proposed, mainly including sequential hydration and dehydrogenation steps in alkaline solution.

The superior catalytic activity NiCoMn-LDHs nanosheets were mainly attributed to: (1) the controllable synthesis of the ultrathin nanosheets (1.15 nm) provided larger contact area with reactant (HMF or furfural) and exposed more oxygen vacancies; (2) the rich covalent of Mn promoted the biomass oxidation reaction rather than water oxidation; (3) the cooperative effect of Ni, Co and Mn enhanced the catalytic performance; (4) the unique and stable structure of LDHs ensured the high efficiency in the process of biomass monomer adsorption and conversion. This work offers a valid strategy to fabricate thin nanosheets that are efficient for the eco-friendly upgrading of the biomass-derived platform chemicals into highly value-add products at atmospheric pressure.

Author Contributions

Conceptualization, K.Y.; Methodology and experiments, B.Y.L., M.Z., Y.Q.L., X.L. and S.J.X.; Writing – original draft, B.Y.L., S.J.X., and Y.C.W; Writing – review & editing, D. D., E. K. G., C. R. A. C., and K. Y.

Conflicts of interest

There are no conflicts to declare.

Acknowledgements

This work was supported by National Natural Science Foundation of China (22078374, 21776324), Guangdong Basic and Applied Basic Research Foundation (2019B1515120058, 2020A1515011149), National Key R&D Program of China (2018YFD0800700), National Ten Thousand Talent Plan, Key-Area Research and Development Program of Guangdong Province (2019B110209003), the Fundamental Research Funds for the Central Universities (19lgzd25) and Hundred Talent Plan (201602) from Sun Yat-sen University. We also thank Diamond Light Source for access to the Beamlines B22 and also acknowledge Diamond Light Source beamline staff and the UK catalysis Hub Block Allocation Group (BAG) Programme Mode Application, in particular Dr. Veronica Celorrio and Dr. June Callison, for provision of beamtime at B18 (Experiment SP19850-9) for collection of the data and the initial discussion. The UK Catalysis Hub is kindly thanked for resources and support provided *via* our membership of the UK Catalysis Hub Consortium and funded by EPSRC grant EP/K014706/2.

References

1. J. C. Serrano-Ruiz, R. Luque and A. Sepúlveda-Escribano, *Chem. Soc. Rev.*, 2011, **40**, 5266-5281.
2. K. Yan, Y. Liu, Y. Lu, J. Chai and L. Sun, *Catal. Sci. Technol.*, 2017, **7**, 1622-1645.
3. G. Guan, M. Kaewpanha, X. Hao and A. Abudula, *Renew. Sust. Energ. Rev.*, 2016, **58**, 450-461.
4. A. J. J. E. Eerhart, A. P. C. Faaij and M. K. Patel, *Energy Environ. Sci.*, 2012, **5**, 6407-6422.
5. Z. Zhang and K. Deng, *ACS Catal.*, 2015, **5**, 6529-6544.
6. M. Sajid, X. Zhao and D. Liu, *Green Chem.*, 2018, **20**, 5427-5453.
7. P. L. Arias, J. A. Cecilia, I. Gandarias, J. Iglesias, M. López Granados, R. Mariscal, G. Morales, R. Moreno-Tost and P. Maireles-Torres, *Catal. Sci. Technol.*, 2020, **10**, 2721-2757.
8. M. Kim, Y. Su, A. Fukuoka, E. J. M. Hensen and K. Nakajima, *Angew. Chem. Int. Ed.*, 2018, **57**, 8235-8239.
9. G. Papanikolaou, P. Lanzafame, S. Perathoner, G. Centi, D. Cozza, G. Giorgianni, M. Migliori and G. Giordano, *Catal. Commun.*, 2021, **149**, 106234.
10. Z. Zhang, J. Zhen, B. Liu, K. Lv and K. Deng, *Green Chem.*, 2015, **17**, 1308-1317.
11. F. Liguori, P. Barbaro and N. Calisi, *ChemSusChem*, 2019, **12**, 2558-2563.
12. D. K. Mishra, H. J. Lee, J. Kim, H.-S. Lee, J. K. Cho, Y.-W. Suh, Y. Yi and Y. J. Kim, *Green Chem.*, 2017, **19**, 1619-1623.
13. F. Kerdi, H. Ait Rass, C. Pinel, M. Besson, G. Peru, B. Leger, S. Rio, E. Monflier and A. Ponchel, *Appl. Catal. A-Gen.*, 2015, **506**, 206-219.
14. M. Douthwaite, X. Huang, S. Iqbal, P. J. Miedziak, G. L. Brett, S. A. Kondrat, J. K. Edwards, M. Sankar, D. W. Knight, D. Bethell and G. J. Hutchings, *Catal. Sci. Technol.*, 2017, **7**, 5284-5293.
15. D. J. Chadderdon, L. Xin, J. Qi, Y. Qiu, P. Krishna, K. L. More and W. Li, *Green Chem.*, 2014, **16**, 3778-3786.
16. P. Parpot, A. P. Bettencourt, G. Chamoulaud, K. B. Kokoh and E. M. Belgsir, *Electrochim. Acta*, 2004, **49**, 397-403.
17. B. You, X. Liu, N. Jiang and Y. Sun, *J. Am. Chem. Soc.*, 2016, **138**, 13639-13646.
18. B. You, N. Jiang, X. Liu and Y. Sun, *Angew. Chem. Int. Ed.*, 2016, **55**, 9913-9917.
19. N. Jiang, X. Liu, J. Dong, B. You, X. Liu and Y. Sun, *ChemNanoMat*, 2017, **3**, 491-495.
20. N. Jiang, B. You, R. Boonstra, I. M. Terrero Rodriguez and Y. Sun, *ACS Energy Lett.*, 2016, **1**, 386-390.
21. Q. Wang and D. O'Hare, *Chem. Rev.*, 2012, **112**, 4124-4155.
22. W.-J. Liu, L. Dang, Z. Xu, H.-Q. Yu, S. Jin and G. W. Huber, *ACS Catal.*, 2018, **8**, 5533-5541.
23. X. Deng, X. Kang, M. Li, K. Xiang, C. Wang, Z. Guo, J. Zhang, X.-Z. Fu and J.-L. Luo, *J. Mater. Chem. A*, 2020, **8**, 1138-1146.
24. X. Li, X. Hao, A. Abudula and G. Guan, *J. Mater. Chem. A*, 2016, **4**, 11973-12000.
25. R. Li, Y. Liu, H. Li, M. Zhang, Y. Lu, L. Zhang, J. Xiao, F. Boehm and K. Yan, *Small Methods*, 2019, **3**, 1800344.
26. B. Liu, M. Zhang, Y. Wang, Z. Chen and K. Yan, *J. Alloys Compd.*, 2021, **852**, 156949.
27. M. Zhang, Y. Liu, B. Liu, Z. Chen, H. Xu and K. Yan, *ACS Catal.*, 2020, **10**, 5179-5189.
28. K.-J. Tsai, C.-S. Ni, H.-Y. Chen and J.-H. Huang, *J. Power Sources*, 2020, **454**, 227912.

29. H. C. Chen, Y. Qin, H. Cao, X. Song, C. Huang, H. Feng and X. S. Zhao, *Energy Stor. Mater.*, 2019, **17**, 194-203.
30. S. Singh, N. M. Shinde, Q. X. Xia, C. V. V. M. Gopi, J. M. Yun, R. S. Mane and K. H. Kim, *Dalton Trans.*, 2017, **46**, 12876-12883.
31. Y. Zhao, T. Sun, Q. Yin, J. Zhang, S. Zhang, J. Luo, H. Yan, L. Zheng, J. Han and M. Wei, *J. Mater. Chem. A*, 2019, **7**, 15371-15377.
32. A. Seijas-Da Silva, R. Sanchis-Gual, J. A. Carrasco, V. Oestreicher, G. Abellán and E. Coronado, *Batteries Supercaps*, 2020, **3**, 499-509.
33. L. Li, R. Ma, Y. Ebina, N. Iyi and T. Sasaki, *Chem. Mater.*, 2005, **17**, 4386-4391.
34. W. Ma, R. Ma, C. Wang, J. Liang, X. Liu, K. Zhou and T. Sasaki, *ACS Nano*, 2015, **9**, 1977-1984.
35. C. Liu, M. Zhang, G. Pan, L. Lundehøj, U. G. Nielsen, Y. Shi and H. C. B. Hansen, *Appl. Clay Sci.*, 2019, **177**, 82-90.
36. S. Nayak, L. Mohapatra and K. Parida, *J. Mater. Chem. A*, 2015, **3**, 18622-18635.
37. L. Wu, J. Hong, Q. Zhang, B.-Y. Chen, J. Wang and Z. Dong, *Chem. Eng. J.*, 2020, **385**, 123620.
38. Y. Tang, H. Shen, J. Cheng, Z. Liang, C. Qu, H. Tabassum and R. Zou, *Adv. Funct. Mater.*, 2020, **30**, 1908223.
39. R. Liu, Y. Wang, D. Liu, Y. Zou and S. Wang, *Adv. Mater.*, 2017, **29**, 1701546.
40. K. Hu, M. Zhang, B. Liu, Z. Yang, R. Li and K. Yan, *Mol. Catal.,* 2021, **504**, 111459.
41. X. Zhang, Y. Zhao, Y. Zhao, R. Shi, G. I. N. Waterhouse and T. Zhang, *Adv. Energy Mater.*, 2019, **9**, 1900881.
42. J.-X. Huang, B. Li, B. Liu, B.-J. Liu, J.-B. Zhao and B. Ren, *J. Power Sources*, 2016, **310**, 85-90.
43. C.-Y. Li, Y. Yu, C. Wang, Y. Zhang, S.-Y. Zheng, J.-F. Li, F. Maglia, R. Jung, Z.-Q. Tian and Y. Shao-Horn, *J. Phys. Chem. C*, 2020, **124**, 4024-4031.
44. M. W. Louie and A. T. Bell, *J. Am. Chem. Soc.*, 2013, **135**, 12329-12337.
45. J. Cao, J. Li, L. Li, Y. Zhang, D. Cai, D. Chen and W. Han, *ACS Sustain. Chem. Eng.*, 2019, **7**, 10699-10707.
46. X. Huang, J. Song, M. Hua, Z. Xie, S. Liu, T. Wu, G. Yang and B. Han, *Green Chem.*, 2020, **22**, 843-849.
47. A. M. Román, N. Agrawal, J. C. Hasse, M. J. Janik, J. W. Medlin and A. Holewinski, *J. Catal.*, 2020, **391**, 327-335.
48. X. Li, G.-Q. Han, Y.-R. Liu, B. Dong, W.-H. Hu, X. Shang, Y.-M. Chai and C.-G. Liu, *ACS Appl. Mater. Interfaces*, 2016, **8**, 20057-20066.
49. L. Trotochaud, J. K. Ranney, K. N. Williams and S. W. Boettcher, *J. Am. Chem. Soc.*, 2012, **134**, 17253-17261.
50. Y. K. Penke, G. Anantharaman, J. Ramkumar and K. K. Kar, *ACS Appl. Mater. Interfaces*, 2017, **9**, 11587-11598.
51. H. Wang, Y. Wang, L. Tan, L. Fang, X. Yang, Z. Huang, J. Li, H. Zhang and Y. Wang, *Appl. Catal. B-Environ.*, 2019, **244**, 568-575.
52. A. Wang, H. Wang, H. Deng, S. Wang, W. Shi, Z. Yi, R. Qiu and K. Yan, *Appl. Catal. B-Environ.*, 2019, **248**, 298-308.
53. N. Zhang, Y. Zou, L. Tao, W. Chen, L. Zhou, Z. Liu, B. Zhou, G. Huang, H. Lin and S. Wang, *Angew. Chem. Int. Ed.*, 2019, **58**, 15895-15903.
54. P. Gallezot, *Chem. Soc. Rev.*, 2012, **41**, 1538-1558.